Fatigue fracture and probabilistic assessments of a cone and pipe welded structure of stainless steels

Gyoko Oh
Research and Experiment Department, Tokyo Roki Co., Ltd.,
1-9-1 Tana Shioda, Chuo-ku, Sagamihara 252-0245, Japan
E-mail address: ou2350@roki.co.jp

Abstract

Using thin-walled cone-pipe welded joints of stainless steels, fatigue tests under bending loads were carried out. The test data were statistically analyzed with the Benard's approximation, Gaussian, 2P-Weibull, and 3P-Weibull distributions. Stress–life curves at different failure probabilities by a constant strength scatter band model were obtained. The metallographic structures were investigated, and the stress concentration states were analyzed to elucidate the causes of the strengths and scatters. In the high-cycle fatigue regime, the 3P-Weibull distribution was mostly in agreement with the Benard's approximation, and the coefficient of determination was 0.9642. The microstructure of the weld metal with a high weld opening angle was mainly ferrite phase with 20% austenite distribution. The crack initiation point was close to the weld interface, but the propagation direction was at a right angle, and initially penetrated the heat affected zone of the cone, leading to the high fatigue strength. The stress concentration factors depended on the weld opening angles, indicating the main factor which affected strengths and scatters.

Keywords: Stainless steel, Weld, Fatigue, Statistical assessment, Microstructure, Stress concentration

1. Introduction

Stainless steel welded structures are widely used in engineering applications due to their excellent properties of corrosion and oxidation resistances [1–4]. Exhaust gas after-treatment devices of internal combustion engines are usually products with vessel shapes which are formed by welding together the molded pieces of thin stainless steel sheets. For example, the endplates of a catalyst muffler body have cone shapes, and in many cases are jointed with inlet and tail pipes through a lap welding process. These welds have complicated geometrical shapes which induce stress concentrations and weld interfaces which induce non-uniform

metallic structures, leading to large scatters in the strength of the structural body. Moreover, to meet the recent exhaust gas regulations, urea aqueous solutions are being injected into the inlet pipe of a catalyst muffler for reducing nitride oxidations, but corrosion problems arose in the device. To improve the corrosion resistance, high chromium stainless steels are being applied but the strength properties and influence factors are needed to be elucidated [3–6].

The fatigue strength and life are influenced not only by the design shape, but also by the scatters in the material lot, manufacturing processes and conditions, etc. Statistical treatment of the data and a large number of samples are necessary to obtain reliable test results. In the recommendations or standards of the WII and ASTM etc., a minimum of ten samples is needed for obtaining stress–life diagrams (or *S*–*N* curves), and a minimum of six samples at each loading level for two or more stages is recommended for evaluating scatters [4–6]. The *S*–*N* curves are plotted in two logarithmic coordinates, and regression lines are drawn with logarithmic values by means of the least squares method.

For simplification, the slope of curves, *m*, is assumed to be a constant, and the variances of logarithmic values of the strength and life are evaluated based on the Gaussian distribution in many cases, that is, the fatigue life and strength are assumed to be log-normally distributed. This means that the strength heteroscedasticity across cycles is assumed, and the strength scatter (standard deviation) increases accordingly when the number of cycles becomes lower. At the same time, many experimental results showed different data plots from this assumption when the material and structure were the same [7–13]. For an extreme instance, it is known that the scatter of tensile strength (equivalent to one quarter of a cycle) is significantly smaller than that of the fatigue strength or limit [6–9]. Meanwhile, eight typical regression models for *S*–*N* curves have been suggested in the JSMS (The Society of Materials Science, Japan) standard, which including the semi-logarithmic bilinear, semi-logarithmic hyperbola, double-logarithmic hyperbola etc., besides the double-logarithmic bilinear [8,11]. Consequently various strength distributions can be presumed depending on materials, test conditions, and data states.

Since the fatigue cracks in a material or structure generally initiate from defects, impurities, and geometrical discontinuities, the weakest link theory has been proposed and the Weibull distribution is widely approved besides the Gaussian distribution [8–12]. In the case of that the spread of test strength points shows homoscedasticity across cycles in the high-cycle fatigue regime (HCF), the scatter of fatigue strengths, but not of logarithmic values, can be presumed to be a constant. This presumption of the homogeneity of variance in fatigue

strength, namely the constant strength scatter band model, has been reasonably proposed in the previous studies [3,11,14]. This simplified method is appropriate for the strength evaluation and accuracy with a limited number of test samples, concerning the structural reliability and integrity in engineering applications.

In this study, thin-walled cone-pipe welded joints of stainless steels which are generally employed for catalyst mufflers are used to carry out fatigue tests under bending loads to plot curves of the fatigue strength and life. In the HCF regime, the scatter of the fatigue strengths is presumed to be a constant, since elastic deformations of a specimen in whole are dominant, and since the test data points show homoscedasticity across cycles [7–14]. The test data are statistically analyzed with the Benard's approximation of the median rank method, Gaussian, 2P-Weibull, and 3P-Weibull distributions. Fatigue strength curves at 50% and 5% failure probabilities by the constant strength scatter band model are obtained for comparison [14]. The metallographic structures are observed, and the stress concentration states are analyzed to elucidate influential factors of the strengths and scatters.

2. Materials and methods

2.1 Specimens and fatigue tests

The specimens were a welded structure as shown in Fig. 1. The inlet part of a catalyst muffler was modeled, and a flange was welded to the shell of 240 mm diameter body for bolting to the test pedestal. The pipe portion of 80 mm diameter was fabricated from a sheet of standard thickness 1.5 mm made of high chromium ferritic steel of 30%Cr–2%Mo (similar to JIS SUS447) with high corrosion resistance. The cone portion was fabricated by plastic forming from a sheet of standard thick 2 mm made of 17%Cr–1%Mo ferritic steel (similar to AISI 436 or JIS SUS436L). The mechanical properties of the cone material were as follows: tensile strength 451 MPa, 0.2% proof stress 289 MPa, elongation 35%, and fatigue strength 331 MPa for 5×10^5 cycles by bending fatigue tests. These two portions were jointed through an automatic metal inert gas lap welding, using a welding wire of 1.2 mm diameter of 24%Cr–14%Ni austenitic steel (similar to AISI 309 or JIS SUS309L). The welded specimens were supplied to the tests without heat treatment.

The fatigue tests were under bending loads as shown in Fig. 1a. The fatigue test machine was an oil pressure servo actuator with a capacity of 12 kN. The tests were carried out under a stroke control of sinusoidal wave loads of 10 Hz frequency. Several strain gauges of 2 mm effective length were attached to the outside surface near the target weld bead where the

maximum loading would be applied, to measure the strains and to stop the tests by interlocks when cracks occurred. The applied loads were measured with a load cell.

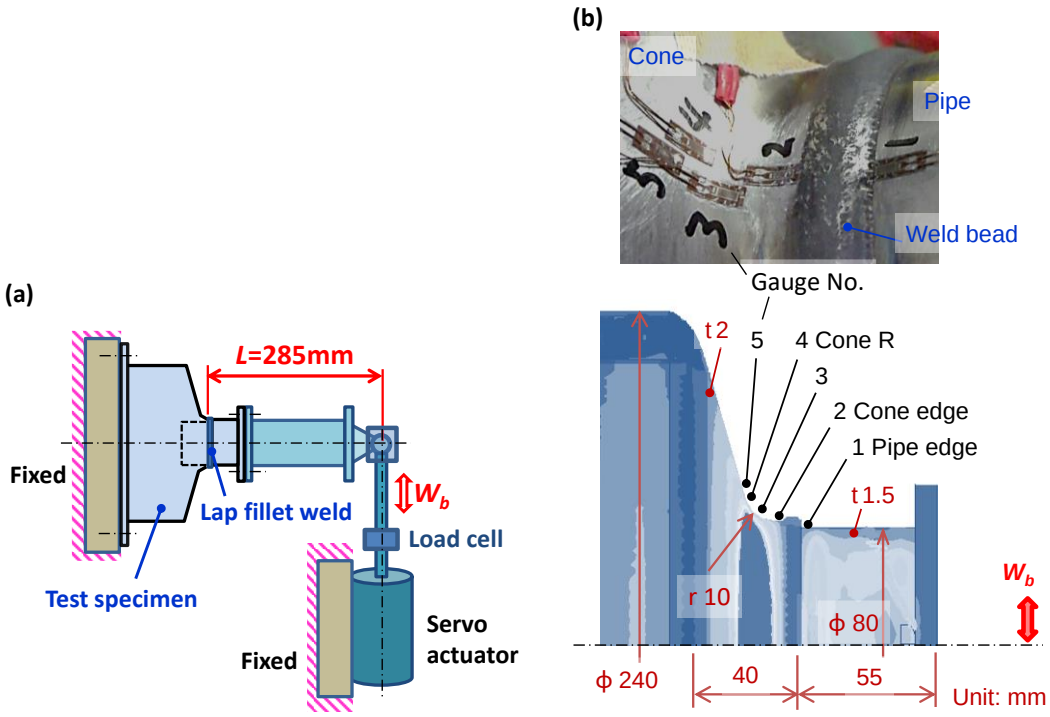

Fig. 1 Outline of the fatigue test for bending load in (a), and specimen dimensions and strain gauge positions in (b).

2.2 Statistical analysis process

The test data were statistically analyzed in the case of the bending fatigue test according to the following process.

1) The measured loading amplitudes M_a and cycles to failure N_f by the fatigue tests were plotted in the *M*–*N* relationship.
2) All plots between 9×10^4 – 2×10^6 cycles in the HCF regime were regressed as a baseline by means of the least squares method. The strength coefficient C_M and strength exponent m were obtained based on the Basquin's power equation of $M_a = C_M N_f^{-1/m}$ [13–17].
3) The test data points show homoscedasticity of the strengths across cycles, rather than that of the logarithmic strengths. The strength difference ΔM_i between this base line and every plotted point was assumed as a constant value, namely the constant strength scatter band model, and translated into the point of 5×10^5 parallel to the base line to obtain the corresponding strength M_i [14]. The translation equation was $M_i = M_a + \Delta M_i$.

4) These strengths of M_i were treated with the Gaussian, 2P-Weibull, and 3P-Weibull distributions in comparison with the failure probability P_{fi} based on the Benard's approximation. The probability density P_d and cumulative failure probability P_f at 5×10^5 cycles were obtained [8–12].
5) Based on the points of $P_f = 0.5$ and $P_f = 0.05$, several strengths at $10^5 - 2\times10^6$ cycles were calculated according to the base line using a constant strength difference. These points were regressed by means of the least squares method and the curves of $P_f = 0.5$ and $P_f = 0.05$ were obtained with the power approximation.
6) The strengths at 2×10^6 cycles were used as the fatigue limits of M_w.
7) Using the relation curves of M_a and measured strain amplitudes, as well as using Hooke's law, the stress amplitudes of S_a were converted. The *P–S–N* diagrams of the failure stress and the number of cycles were obtained.

2.3 Metallographic structure analyses

After the fatigue tests, some fractured specimens were cut out, polished, and etched for 2–3 minutes with a mixed solution of the nitric acid 3 and hydrochloric acid 1. The sectional metallographic structures were observed through a metaloscope. The chemical compositions were analyzed through a scanning electron microscope combining with an energy dispersive X-ray spectroscopy (SEM-EDS), and the phase contents were identified based on the Schaeffler's diagram [20].

2.4 Numerical stress analyses

The elastic stresses were analyzed with a two dimension finite element method (FE) using the sectional models of fatigue failure portions of specimens, to compare their stress concentration states near the crack initiation points. Fig. 2 shows the analysis models with a unit thickness and meshes. P_C is the cone, P_P the pipe, and P_W the weld portion in (a). Two ends of the sectional portion near the welding bead of models were restrained in the vertical direction, and the unit load F was applied at two points of the model in the downward direction. In this loading state of four-point bending, the load distribution was a constant between the two loading points. Several models of the unfractured portion of the specimen (b), the cracked portion (c) of the high strength specimen A_H, and the cracked portion (d) of the low strength specimen A_L were computed, and the stress concentration states were compared. Triangle meshes were used. The mesh sizes near the crack initiation point were about 0.1 mm, and others were 0.1 – 0.3 mm. Using the linear element, the computed stress was an averaged

value in one element. With presuming a homogeneous material, the Young's modulus was 206 GPa and Poisson's ratio was 0.3.

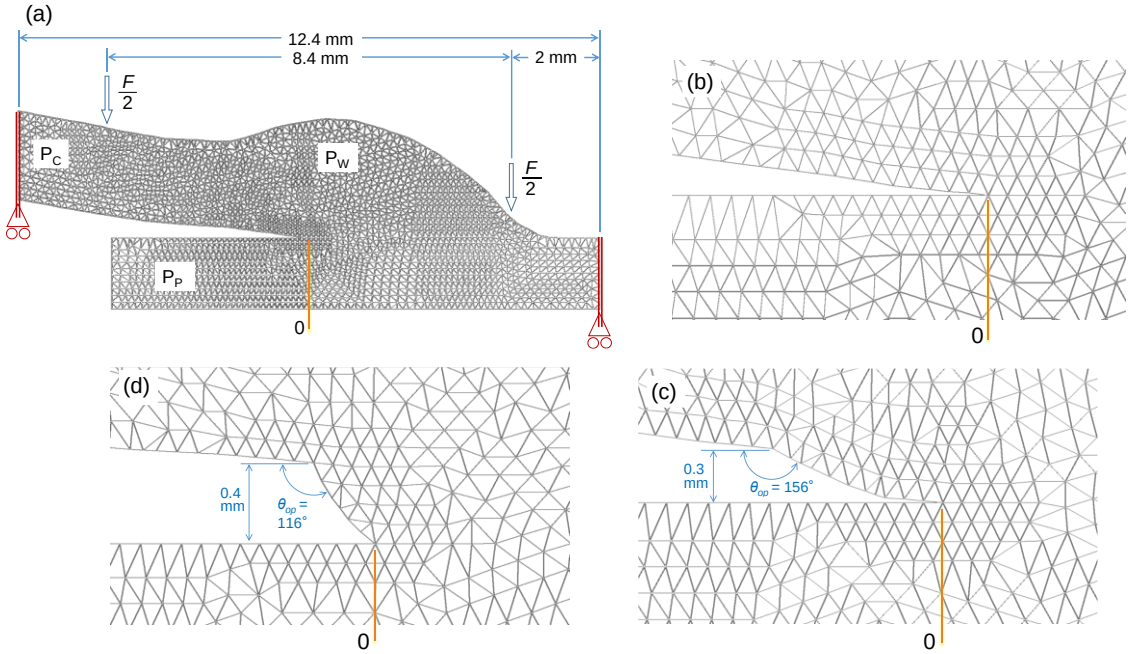

Fig. 2 FE analysis models and meshes. P_C is the cone, P_P the pipe, and P_W the weld portion in (a). (b) is the unfractured portion enlargement near the point 0. (c) and (d) are specimens $A_{H(156)}$ and $A_{L(116)}$.

3. Experimental and numerical results and discussion

3.1 Bending fatigue strengths

From the loading amplitude W_b and the distance to the fractured point L, the bending moment amplitude due to the load was $M_a = LW_b$. Using the measured surface strain amplitude ε_a with the strain gauges and the Young' modulus E = 206 GPa, the stress amplitude was calculated based on $S_a = E\varepsilon_a$ according to Hooke's law. As shown in Fig. 3a, when W_b is raised stepwise, the S_a rises proportionally, and the maximum stress amplitude at the curved portion of the cone (cone R) had a relationship of $S_a = 0.6076M_a$ from the regression line by means of the least squares method. This line had excellent linearity, and the coefficient of determination R^2 was 0.9997, showing that elastic deformations were dominant in whole.

In comparison at M_a = 490 Nm, the strain gauge 4 shows the maximum value of the stress amplitude as shown in Fig. 3b. This converted stress amplitude from the strain gauge 4 was used as the representative stress amplitude S_a of the specimens. The converted stress amplitude of the strain gauge 2 at the corresponding outside point of the cone edge was low,

because the fatigue cracks initiated from the internal portion as described below. The nominal stress amplitude could be calculated from the ring section modulus of the cone edge, and it was close to the converted stress amplitudes of the strain gauges 1 and 2.

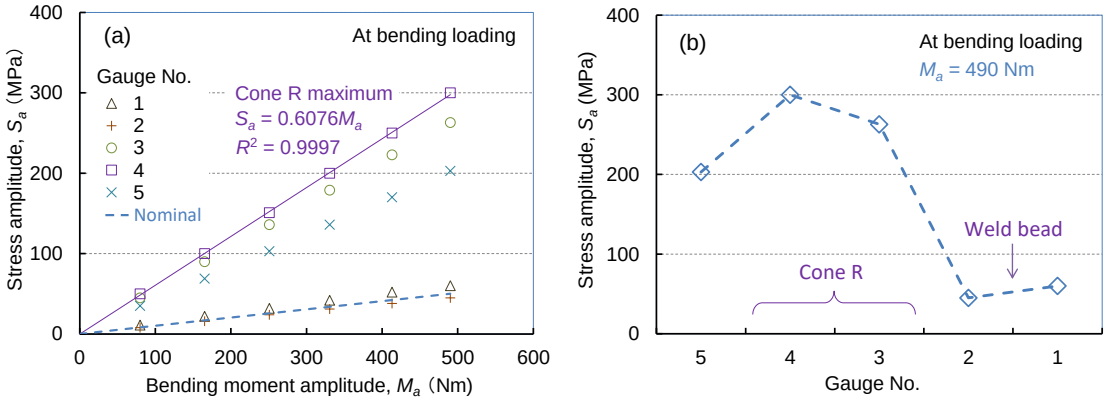

Fig. 3 Relationships between stress amplitudes and bending moment amplitudes in (a), and values according to strain gauge positions in (b).

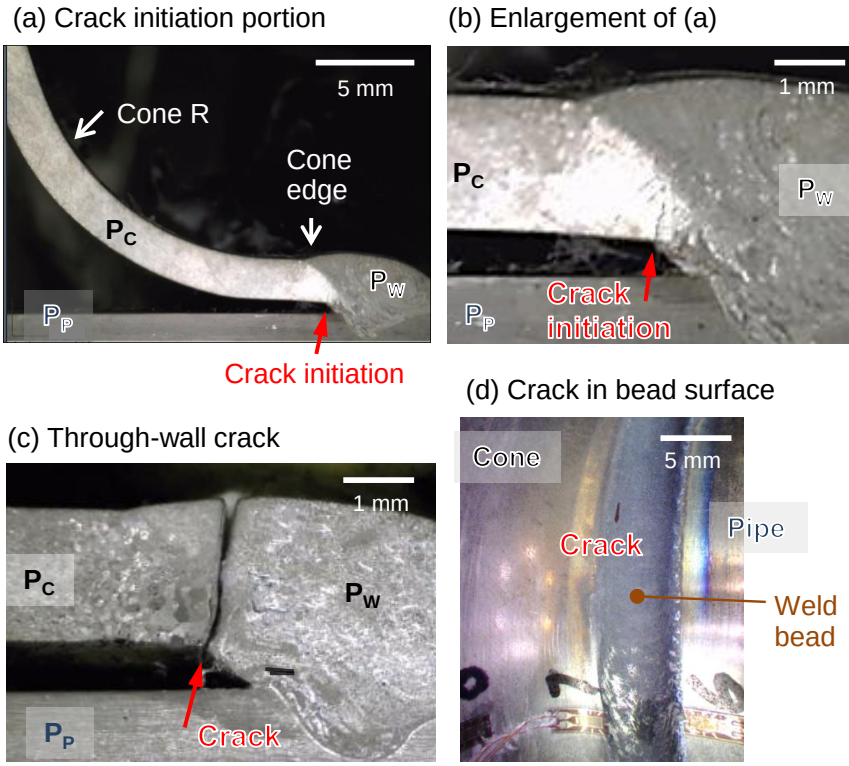

Fig. 4 Crack positions after fatigue tests in the HCF regime. (a) and (b) show the internal portion crack initiation of the cone edge. (c) shows the through-wall crack, and (d) shows the crack in the weld bead surface immediately after penetrating the wall.

The fatigue crack position was different by the loading level. Under the load higher than 600 Nm, the crack occurred in the curved portion of the cone. Under this high level load, the

surface stress amplitude exceeded the 0.2% proof stress from the following measured results. It is considered that the surface plastic strains occurred, leading to the low-cycle fatigue failures (LCF, $N_f < 5\times10^4$ cycles). Under the load of lower than 600 Nm, the failure became the HCF cycle regime. The fatigue cracks initiated from the internal portion of the cone edge as shown in Figs. 6a and 6b, and then propagated to the weld bead surface through the wall as shown in Figs. 6c and 6d.

When the crack occurred in the test, the measured strains varied, and the loading value also became lower than the initial value due to the stroke control. The test was stopped through an interlock at set values, and a dye penetrant testing was carried out. When the surface coloration occurred as shown in Fig. 4b, the test was stopped and the number of cycles was used as the failure cycles. Under the load lower than 600 Nm, the cracks of almost all specimens initially penetrated the wall when the measured loads became lower than the initial applied load by 3%, and therefore the corresponding cycles were adopted as the fracture criteria.

The failure points in the fatigue tests were plotted with the *M*–*N* coordinates as shown in Fig. 5a. All plots between 9×10^4 – 2×10^6 cycles in the HCF regime were regressed as a baseline by means of the least squares method, and the strength coefficient C_M and strength exponent m were obtained based on the Basquin's power equation of $M_a = C_M N_f^{-1/m}$ [17–23]. The least squares method was expressed in the following equation, and the calculation was carried out on the condition that the δ became the minimum.

$$\delta = \sum_{i=1}^{n} (M_i - C_M N_f^{-\frac{1}{m}})^2 \qquad (1)$$

Using 2×10^6 cycles as the knee point, the fatigue limit M_w was obtained. This M_w corresponds to the intermediate horizontal line between the fractured and unfractured points at 2×10^6 – 10^7 cycles. The strength difference ΔM_i between the regressed base line and every plotted point was assumed as a constant value, and translated into the point of 5×10^5 parallel to the base line to obtain the corresponding strength M_i. These strengths of M_i were treated with the Gaussian, 2P-Weibull, and 3P-Weibull distributions in comparison with the failure probability P_{fi} based on the Benard's approximation. The cumulative failure probability P_f at 5×10^5 cycles were expressed by the following equations:

Benard : $$P_{fi} = (i - 0.3)/(n + 0.4) \qquad (2)$$

Gaussian : $$P_f = \{1 + \mathrm{erf}[(M_a - \mu)/(\sqrt{2}S_D)]\}/2 \qquad (3)$$

2P-Weibull: $$P_f = 1 - \exp[-(M_a/\beta)^{\alpha}] \qquad (4)$$

3P-Weibull: $P_f = 1 - \exp\{-[(M_a - \gamma)/\beta]^{\alpha}\}$ (5)

where i is the number of the cumulative failure, n the total number of specimens, erf the error function, μ the mean, S_D the standard deviation, α the shape parameter, β the scale parameter, and γ the threshold parameter. The equations for calculating the probability density function denoted as P_d were expressed by the following equations [8,9,14]:

Gaussian : $P_d = \exp[-(M_a - \mu)^2/(2{S_D}^2)]/(\sqrt{2}S_D)$ (6)

2P-Weibull: $P_d = \alpha {M_a}^{\alpha-1} \exp[-(M_a/\beta)^{\alpha}]/\beta^{\alpha}$ (7)

3P-Weibull: $P_d = \alpha {M_a}^{\alpha-1} \exp\{-[(M_a - \gamma)/\beta]^{\alpha}\}/\beta^{\alpha}$ (8)

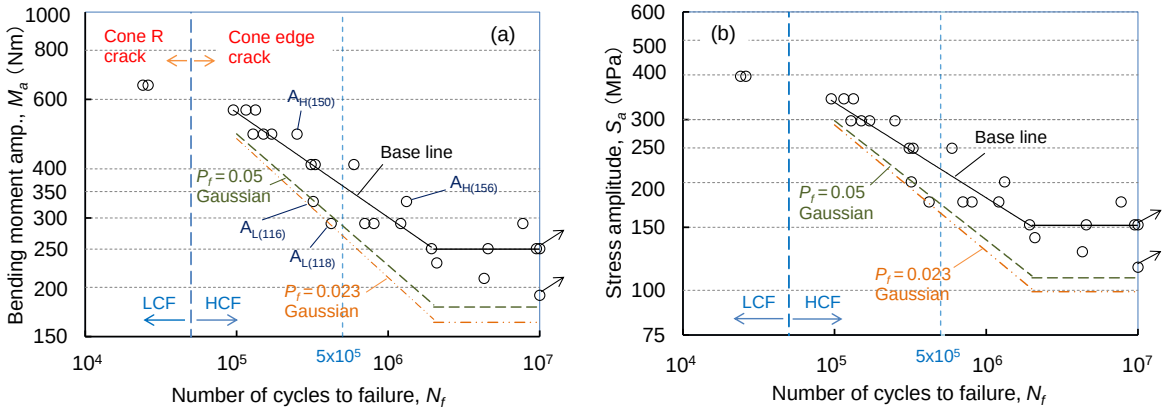

Fig. 5 *P–M–N* diagram (a) and *P–S–N* diagram (b) from bending fatigue tests.

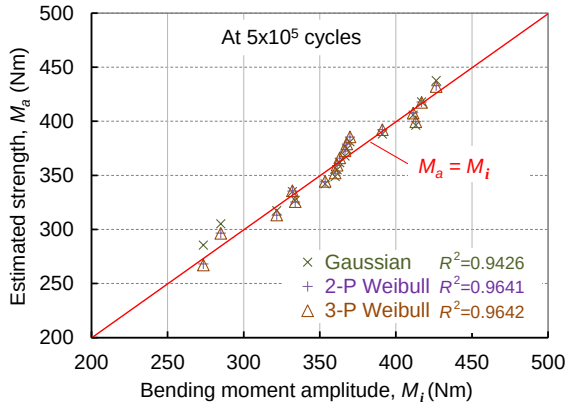

Fig. 6 Relationships between M_i by the Benard's approximation and M_a by the probabilistic distributions in the HCF regime.

As shown in Fig. 6, the regression line between the failure moment amplitude M_i corresponding to the P_{fi} by Benard's approximation and the estimated M_a by the probabilistic distributions was drawn, and the parameters of each probabilistic distribution were determined when they were adjusted to approach $M_a = M_i$ with an error less than 0.1%. The

3P-Weibull distribution strength was mostly in agreement with the Benard's approximation, and the coefficient of determination R^2 was 0.9642.

Based on these parameters, P_f and P_d were obtained and shown in Fig. 7. Based on the points of P_f = 0.5 and P_f = 0.05, several strengths in the HCF regime of 10^5 – 2×10^6 cycles were estimated according to the base line using a constant strength difference. These points were regressed by means of the least squares method and the curves of P_f = 0.5 and P_f = 0.05 were obtained with the power approximation. The differences between the estimated values and the regressed values were less than 2%.

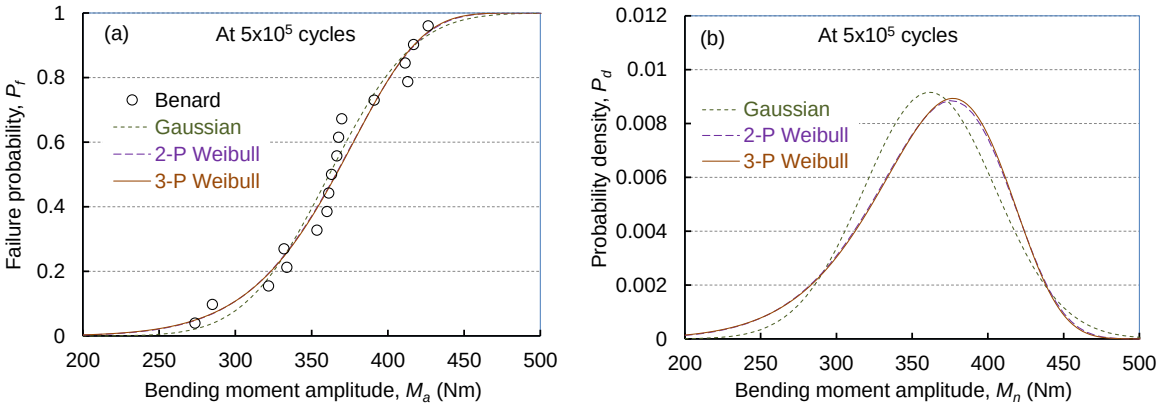

Fig. 7 Failure probabilities and probability densities at 5×10^5 cycles.

Any other P_f lines could be estimated, and this process was defined as the constant strength scatter band model or method for evaluating fatigue strengths. The lines of P_f = 0.05 and P_f = 0.023 (equivalent to $2S_D$) by the Gaussian distribution are added in Fig. 5a. P_f = 0.5 line is the same with the base line. The strengths at 2×10^6 cycles were used as the fatigue limits of M_w, and the horizontal lines of the corresponding P_f were also obtained. Furthermore, using the relation curves of M_a and measured strain amplitudes, as well as using Hooke's law, the stress amplitudes of S_a were converted, and the *P*–*S*–*N* diagrams of the failure stress and the number of cycles were obtained as shown in Fig. 5b.

The calculations for the 2P-Weibull and 3P-Weibull distributions could be carried out in the same way, and their P_f lines were obtained as shown in Fig. 8. At P_f = 0.05 and P_f = 0.5, the strength coefficient C_S and strength exponent m of the Basquin's power equation were listed in Table 1. At P_f = 0.5, every distribution had the same degree of the m, meaning that the slope of the *S*–*N* curves was almost the same. At P_f = 0.05, the m estimated by the 3P-Weibull distribution was the smallest, meaning that the slope of its *S*–*N* curve was steep. Moreover, the estimated strengths at 5×10^5 cycles and the fatigue limits are summarized in

Table 2. The value of the S_a or S_w at P_f = 0.05 by the 3P-Weibull distribution was the lowest, and the scatter band ΔS_a or ΔS_w was the largest. There were no obvious differences between the 2P-Weibull and 3P-Weibull distributions.

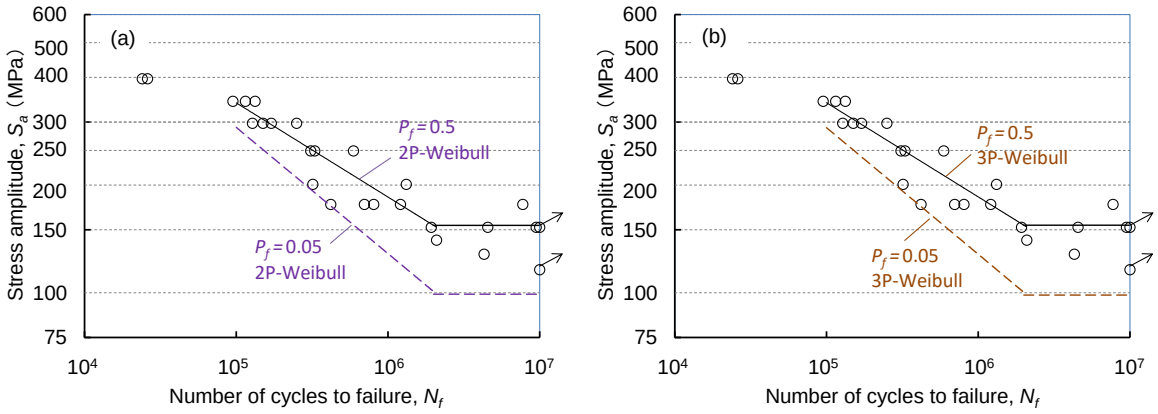

Fig. 8 *P–S–N* diagram based on the 2-P Weibull in (a) and 3-P Weibull distribution in (b).

Table 1 Estimated constants of the Basqiun's equation by probabilistic assessments.

Loading	Distribution	P_f = 0.05			P_f = 0.5		
		C_S	1/m	m	C_S	1/m	m
Bending	Gaussion	13,861	0.334	2.99	7,244	0.266	3.76
	2-P Weibull	16,831	0.353	2.83	7,047	0.263	3.80
	3-P Weibull	17,029	0.354	2.82	7,032	0.263	3.80

Table 2 Estimated fatigue strengths and limits by probabilistic assessments.

Loading	Distribution	S_a at 5×10^5 cycles		ΔS_a	S_w		ΔS_w	$\Delta S_w/S_w$
		P_f = 0.05	P_f = 0.5	P_f 0.05-0.5	P_f = 0.05	P_f = 0.5	P_f 0.05-0.5	P_f = 0.5
		MPa	MPa	MPa	MPa	MPa	MPa	
Bending	Gaussion	176.2	219.7	43.5	108.4	151.8	43.5	0.286
	2-P Weibull	167.0	222.3	55.3	99.1	154.4	55.3	0.358
	3-P Weibull	166.5	222.5	56.0	98.6	154.6	56.0	0.362

3.2 Metallographic structures

Fig. 9 shows the sectional surfaces of cracked specimens etched by the mixed acids through a metaloscope near the crack initiation points of the high strength specimen of $A_{H(156)}$ and the low strength specimen of $A_{L(116)}$ after fatigue tests under the loading of M_a = 331 Nm. The arrows indicate the crack initiation points, and the weld opening angles denoted as θ_{op} at these points were 156° and 116°. The un-cracked portion of the specimens had no angle like these and was about 180°. The specimens were etched for 2–3 minutes with a mixed solution

of the nitric acid 3 and hydrochloric acid 1, and the corrosion resistance of the cone was the lowest. By the welding, the crystal grain sizes in the heat affected zone (HAZ) close to the crack initiation point became about 150 μm from about 20 μm of the initial material. The pipe portions were almost not corroded, giving a desired advantage for improving corrosion resistance of a catalyst muffler device subject to the urea aqueous solution attack during use.

Fig. 10 shows the backscattered electron (BSE), Cr, and Ni distribution images of the above specimens by the SEM-EDS analyses. The analyzed chemical compositions within the cycles of 500 μm diameter were listed in Table 3. Based on the Schaeffler's diagram of phase–chemical composition (chromium and nickel equivalents), the welded metal (P_w2) in the specimen $A_{H(156)}$ had a main phase of ferrite, distributed by 20% phase of austenite. In this specimen, the crack initiation point was close to the weld interface, but the propagation direction was in a right angle to this interface. At the initial stage, the crack propagated through the HAZ of the cone, resulting in the high strength. The welded metal (P_w1–P_w2) in the specimen $A_{L(116)}$ had a mixed phase of half ferrite and half austenite. The crack initiation point was at the weld interface, and the propagation direction was according to this interface, resulting in the low strength.

Table 3 Analyzed chemical compositions and estimated phase contents.

Specimen	Area	Chemical composition (wt.%)								Equivalent		Phase [a]
		C	Cr	Ni	Mo	Ti	Si	Mn	Fe	Cr_{eq}	Ni_{eq}	
$A_{H(156)}$	P_W1	0.004	18.37	1.08	0.85	0.17	0.04	0.00	79.49	19.28	1.21	F
	P_W2	0.012	22.62	6.00	0.62	0.25	0.20	0.18	70.12	23.54	6.44	A+F80%
	P_C	0.003	16.46	0.00	1.12	0.30	0.06	0.00	82.06	17.67	0.09	F
	P_P	0.007	27.82	0.30	2.12	0.32	0.10	0.00	69.33	30.09	0.51	F
$A_{L(116)}$	P_W1	0.011	23.00	8.68	0.34	0.02	0.15	0.92	66.88	23.57	9.48	A+F36%
	P_W2	0.009	21.40	6.58	0.52	0.21	0.26	0.85	70.17	22.31	7.28	A+M+F55%
	P_C	0.003	17.53	0.00	1.02	0.20	0.13	0.00	81.12	18.75	0.09	F
	P_P	0.007	28.54	0.39	1.72	0.12	0.06	0.00	69.16	30.35	0.60	F

[a] F: ferrite, A: austenite, M: martensite.

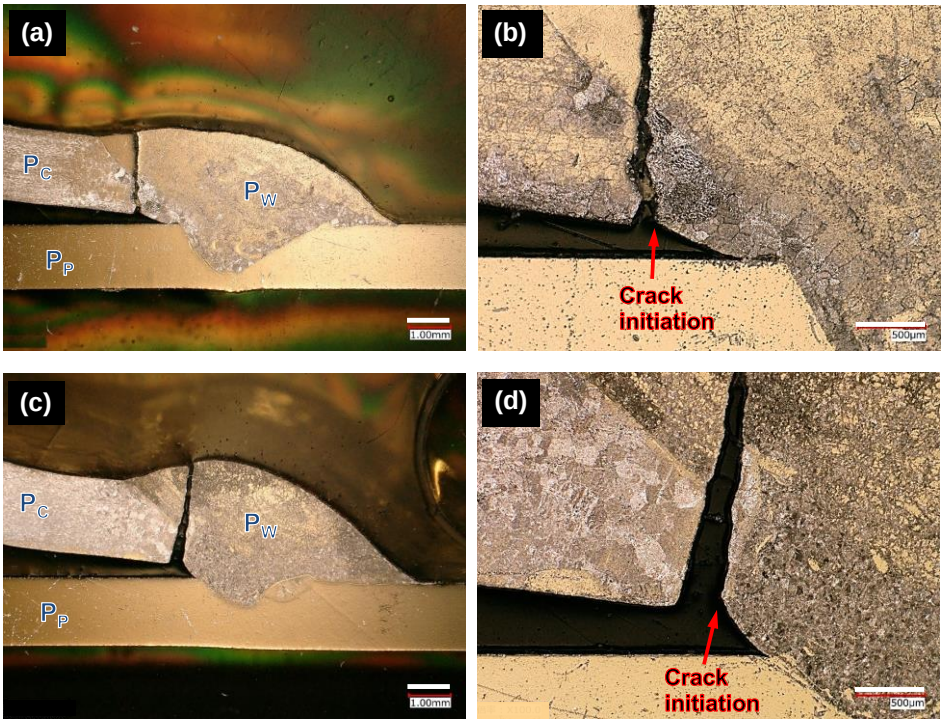

Fig. 9 Sectional surfaces and microstructures of cracked specimens etched by the mixed acids. (a) and (b) are the specimen $A_{H(156)}$ with the high strength and (c) and (d) are $A_{L(116)}$ with the low strength.

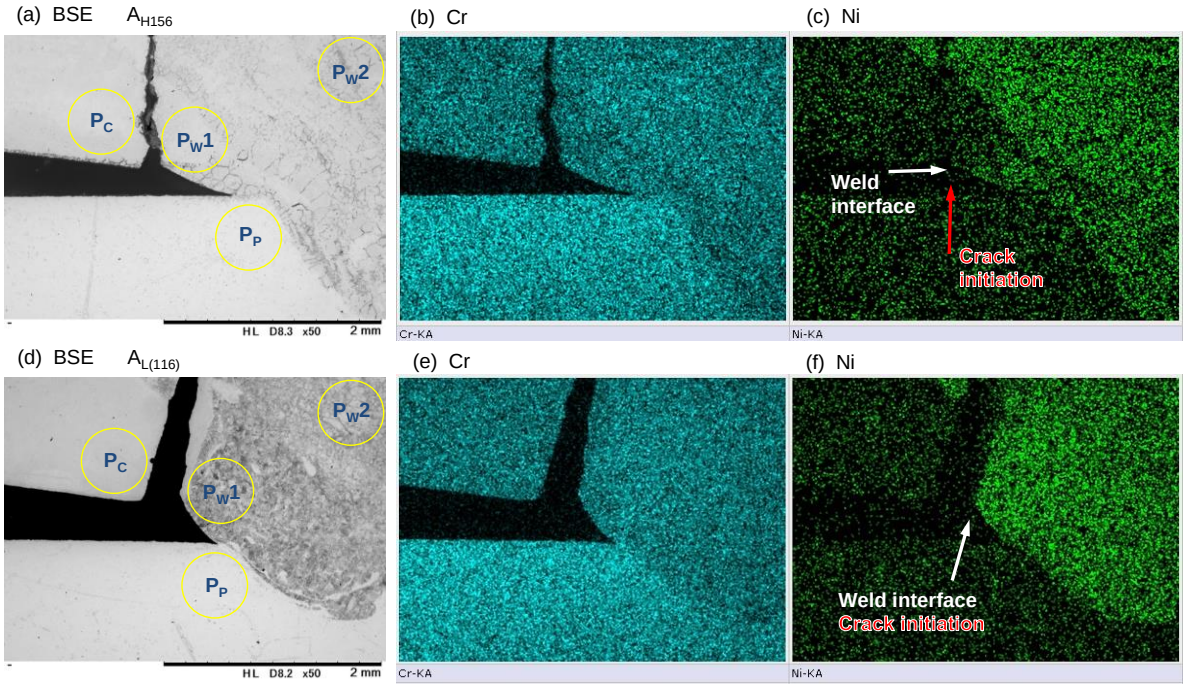

Fig. 10 SEM-EDS analyzed elemental distributions. (a)–(c) are the specimen $A_{H(156)}$, and (d)–(f) are $A_{L(116)}$.

3.3 Stress concentration states

The FE analysis results are shown in Fig. 11. When the gap between the cone and the pipe was small and the weld opening angle was large, the stress concentration occurred at the notch tip of the gap denoted as the 0 point. However, even though a sharp notch at this 0 point existed, it did not become a crack initiation point. The stress level could not be used as the crack initiation criterion, and the stress gradient or the stress intensity factor was lower than the failure criterion at this 0 point [3].

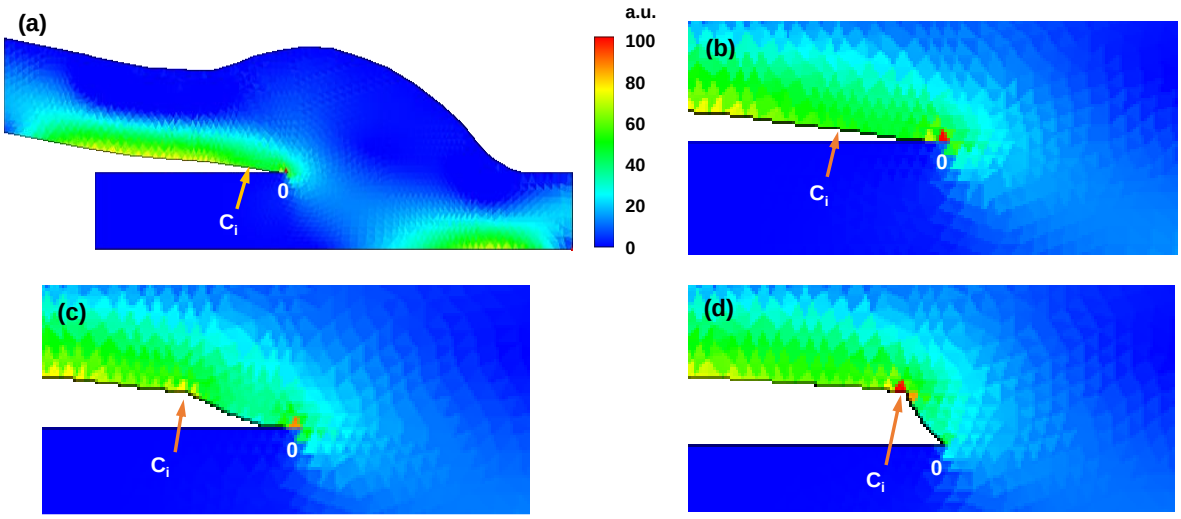

Fig. 11 FE analyzed maximum principal stress distributions in arbitrary unit. (a) and (b) are the unfractured portion of specimen, (c) is the specimen $A_{H(156)}$, and (d) is $A_{L(116)}$.

The stresses of the crack initiation point C_i were focused and analyzed here excluding the 0 point. The concentration factor K_t of the specimen $A_{H(156)}$ was 1.39, and that of the specimen $A_{L(116)}$ was 1.84. Here K_t is the maximum principal stress ratio of the crack initiation point to unfractured portion at the same C_i position. The results of several specimens with different weld opening angles were added, and the relationship between the K_t and θ_{op} can be approximated as:

$$K_t = 1 + \zeta \sin\theta_{op} \quad (9)$$

where ζ is the constant, determined by the weld shape and mesh size. ζ was 0.96 here with the least squares method.

Fig. 12 shows the stress concentration factor and fatigue notch factor according to the weld opening angle. The fatigue strength at 5×10^5 cycles of the specimen $A_{H(156)}$ was 250 MPa, and that of the specimen $A_{L(116)}$ was 173 MPa, corresponding to their fatigue notch factors of k_a = 1.32 and k_a = 1.91. Here K_a is the fatigue strength ratio of the cone material sheet to weld specimen at 5×10^5 cycles. In addition, other measured data of the high strength

specimen $A_{H(150)}$ and low strength specimen $A_{L(118)}$ were summarized in the same Table 4. When defining the material factor as $\eta_a = K_a/K_t$, η_a was within 0.88–1.09 for every specimen, and the average of the specimens was $\eta_a = 0.99$.

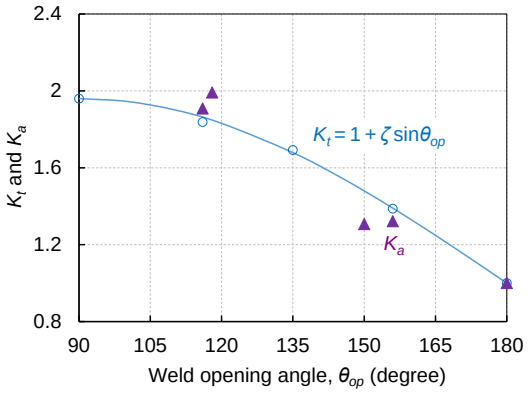

Fig. 12 Stress concentration factor and fatigue notch factor according to the weld opening angle.

Table 4 Stress concentration etc. at the crack initiation point of specimens.

Specimen	θ_{op} Degree	K_t At C_i	S_a MPa	K_a	η_a K_a/K_t
Material sheet	180	1.00	331	1.00	1.00
$A_{H(156)}$	156	1.39	250	1.32	0.95
$A_{H(150)}$	150	1.48	253	1.31	0.88
$A_{L(118)}$	118	1.83	166	1.99	1.09
$A_{L(116)}$	116	1.84	173	1.91	1.04
Average	144	1.51	235	1.51	0.99
S_D	27	0.35	68	0.43	0.08
C_v	18.8%	23.1%	28.8%	28.3%	8.0%

A_H: high strength specimen, A_L: low strength specimen.
S_a: equivalent strength at 5×10^5 cycles.

Since the coefficient of variation C_v for K_t and K_a was close to each other, the stress concentration factor corresponding to the weld opening angles at the C_i portion was suggestively the main influence factor on their strengths and scatters [24–31]. The influences of irregular shapes and metal structures were represented by η_a, which also caused the variations of strengths and scatters.

4. Conclusions

In this study, fatigue tests under bending loads were carried out to investigate fatigue strengths in the HCF regime using the thin-walled cone-pipe welded joints of stainless steels.

The test data were statistically analyzed with the Benard's approximation of the median rank method, Gaussian, 2P-Weibull, and 3P-Weibull distributions. Fatigue strength curves at 50% and 5% failure probabilities by the constant strength scatter band model were obtained for comparison. The metallographic structures were observed, and the stress concentration states were analyzed to elucidate influential factors of the strengths and scatters.

In the HCF regime, the measured stress amplitude was proportional to the bending moment amplitudes, showing that the elastic deformations were dominant in whole. The fatigue cracks initiated from the internal portion of the cone edge, and propagated to the weld bead surface through the wall.

The 3P-Weibull distribution was mostly in agreement with the Benard's approximation, and the coefficient of determination was 0.9642. At P_f = 0.5, every distribution had the same degree of the m, meaning that the slope of the S–N curves was almost the same. At P_f = 0.05, the m estimated by the 3P-Weibull distribution was the smallest, the estimated fatigue limit was the lowest, and the scatter band was the largest.

The microstructure of the weld metal in the joint with a high weld opening angle was mainly ferrite phase with 20% austenite distribution. The crack initiation point was close to the weld interface, but the propagation direction was at a right angle, and initially penetrated the heat affected zone of the cone, leading to the high fatigue strength.

The welded metal in the joint with a low weld opening angle had a mixed phase of half ferrite and half austenite. The crack initiation point was at the weld interface, and the propagation direction was according to this interface, resulting in the low strength.

The stress concentration factors depended on the weld opening angles, indicating the main factor which affected strengths and scatters.

References

1. Hong Y, Miller LJ, Brown MW. Complex stress functions and plastic zone sizes for notch cracks subjected to various loading conditions. Fatig Fract Eng Mater Struct 1991; 14 (2–3): 237–258. https://doi.org/10.1111/j.1460-2695.1991.tb00656.x.
2. Hobbacher A. The new IIW recommendations for fatigue assessment of welded joints and components – A comprehensive code recently updated. Int J Fatigue 2009; 31 (1): 50–58. https://doi.org/10.1016/j.ijfatigue.2008.04.002.
3. Oh G, Sasaki T, Akiniwa Y. Experimental and computational analyses on fatigue fracture and microstructure in dissimilar metal weldments with circular sharp stress raiser. Int J

Fatigue 2020; 133: 105422. https://doi.org/10.1016/j.ijfatigue.2019.105422.

4. Oh G. Bending fatigue and microstructure of fillet welded joints with high chromium stainless pipe for catalyst muffler. SAE Tech Papers 2017; 2017-01-0472. https://doi.org/10.4271/2017-01-0472.
5. ASTM Committee. Standard practice for statistical analysis of linear or linearized stress–life (*S*–*N*) and strain–life (*ε*–*N*) fatigue data. ASTM E739–91(2004), ASTM International, 2004.
6. Tovo R, Livieri P. An implicit gradient application to fatigue of sharp notches and weldments. Eng Fract Mechanics 2007; 74 (4): 515–526. https://doi.org/10.1016/j.engfracmech.2006.06.009.
7. Garcia-Martin R, Bautista-De Castro Á, Sánchez-Aparicio LJ et al. Combining digital image correlation and probabilistic approaches for the reliability analysis of composite pressure vessels. Archiv Civ Mech Eng 2019; 19: 224–239. https://doi.org/10.1016/j.acme.2018.10.001.
8. Sakai T, Nishikawa I. Fundamentals and recent topics on fatigue, V: Databases on fatigue strength and regression method of S-N curves. Zairyo (J Soc Mat Sci, Jpn) 2003; 52 (6): 709–715. https://doi.org/10.2472/jsms.52.709.
9. Weibull W. A statistical distribution function of wide applicability. J Appl Mech (Trans ASME) 1951; 18 (3): 293–297.
10. Qin Y, Besten HD, Palkar S, Kaminski ML, Mid- and high-cycle fatigue of welded joints in steel marine structures: effective notch stress and total stress concept evaluations, Int J Fatigue 2021; 142: 105822. https://doi.org/10.1016/j.ijfatigue.2020.105822.
11. Kuroda M, Sakaida A, Oguma N, Nakagawa M, Matsumura T, Sakai T. Historical review on origin and application to metal fatigue of probit and staircase methods and their future prospects. Zairyo (J Soc Mat Sci, Jpn) 2020; 69 (3): 190–196. https://doi.org/10.2472/jsms.69.190.
12. Bastenaire F. New method for the statistical evaluation of constant stress amplitude fatigue-test results. In: Probabilistic Aspects of Fatigue, Heller R ed. West Conshohocken, PA: ASTM International, 1972; p. 3–28.
13. JIS Committee. General rules for fatigue testing of metals. JIS Z 2273–1978. In: JIS handbook I, Japanese Standard Association, 2020; p. 672–675.
14. Oh G. Fatigue strength distribution and probabilistic evaluation on stainless steel welded components under mixed mode loading. Int J Fatigue 2021; 106247.

https://doi.org/10.1016/j.ijfatigue.2021.106247.

15. Fricke W. Recent developments and future challenges in fatigue strength assessment of welded joints. Proc Inst Mech Engineers Part C: J Mech Eng Sci 2014; 229 (7): 1224–1239. https://doi.org/10.1177/0954406214550015.
16. Mark AF, Francis JA, Dai H, Turski M, Hurrell PR, Bate SK, Kornmeier JR, Withers PJ. On the evolution of local material properties and residual stress in a three-pass SA508 steel weld. Acta Materialia 2012; 60 (8): 3268–3278. https://doi.org/10.1016/j.actamat.2012.03.022.
17. Oh G, Akiniwa Y. Bending fatigue behaviour and microstructure in welded high strength bolt structures. Proc Inst Mech Engineers Part C: J Mech Eng Sci 2019; 233 (10): 3557–3569. https://doi.org/10.1177/0954406218813391.
18. Gough HJ, Pollard HV. The strength of metals under combined alternating stresses. Proc Inst Mech Engineers 1935; 131: 3–103. https://doi.org/10.1243/PIME_PROC_1935_131_008_02.
19. Oh G. Vibration response properties in frame hanging catalyst muffler, SAE Int J Commer Veh 2018; 11 (3): 201–211. https://doi.org/10.4271/02-11-03-0016.
20. Oh G, Akiniwa Y. Residual and assembling stress analyses on fillet welded joints of flange pipes and the fatigue strength prediction. Thin-Walled Struct 2019; 136: 138–149. https://doi.org/10.1016/j.tws.2018.12.011.
21. Niesłony A, Böhm M. Mean stress effect correction using constant stress ratio S–N curves. Int J Fatigue 2013; 52: 49–56. https://doi.org/10.1016/j.ijfatigue.2013.02.019.
22. Mlikota M, Schmauder S, Božić Ž. Calculation of the Wöhler (S-N) curve using a two-scale model. Int J Fatigue 2018; 114: 289–297. https://doi.org/10.1016/j.ijfatigue.2018.03.018.
23. Kucharczyk P, Madia M, Zerbst U, Schork B, Gerwien P, Münstermann S. Fracture-mechanics based prediction of the fatigue strength of weldments: Material aspects. Eng Fract Mechanics 2018; 198: 79–102. https://doi.org/10.1016/j.engfracmech.2017.09.010.
24. Wang X, Ishii H, Sato K: Fatigue and microstructure of welded joints of metal sheets for automotive exhaust system, JSAE Review 2003; 24 (3): 295–301. https://doi.org/10.1016/S0389-4304(03)00041-9.
25. Oh G. Bending fatigue strength and the effect of assembling stress on fillet welded joints of catalyst muffler flange pipes. Int J Automot Eng 2017; 8 (2): 87–94. https://doi.org/10.20485/jsaeijae.8.2_87.

26. Sakaguchi M, Okazaki M. Distinctive role of plastic and creep strain in directional coarsening of a Ni-base single crystal superalloy. Mater Sci Eng A 2018; 710: 121–128. https://doi.org/10.1016/j.msea.2017.10.085.
27. Shimamura Y, Matsushita S, Fujii T, Tohgo K, Akita K, Shobu T, Shiro A. Feasibility study on application of synchrotron radiation μCT imaging to alloy steel for non-destructive inspection of inclusions. Metals 2019; 9 (5): 527. https://doi.org/10.3390/met9050527.
28. Oh G, Akiniwa Y. Mean and residual stress effects on fatigue behavior in a pre-strained corner of stainless steel sheet. Int J Fatigue 2021; 145: 106125. https://doi.org/10.1016/j.ijfatigue.2020.106125.
29. Lynch S. Some fractographic contributions to understanding fatigue crack growth. Int J Fatigue 2017; 104: 12–16. https://doi.org/10.1016/j.ijfatigue.2017.06.036.
30. Sangid MD, Maier HJ, Sehitoglu H. An energy-based microstructure model to account for fatigue scatter in polycrystals. J Mech Phys Solids 2011; 59: 595–609. https://doi.org/10.1016/j.jmps.2010.12.014.
31. Mourad A-HI, Khourshid A, Sharef T. Gas tungsten arc and laser beam welding processes effects on duplex stainless steel 2205 properties. Mater Sci Eng A 2012; 540: 105–113. https://doi.org/10.1016/j.msea.2012.04.012.